

Research



**Cite this article:** Lopez JM, Altmeyer SA. 2023 Arrow-shaped elasto-inertial rotating waves. *Phil. Trans. R. Soc. A* **381**: 20220227. <https://doi.org/10.1098/rsta.2022.0227>

Received: 29 July 2022

Accepted: 23 December 2022

One contribution of 15 to a theme issue 'Taylor–Couette and related flows on the centennial of Taylor's seminal *Philosophical Transactions* paper (Part 2)'.

**Subject Areas:**

fluid mechanics, computational physics, computer modelling and simulation, computational mechanics, applied mathematics, complexity

**Keywords:**

Taylor–Couette flow, viscoelastic fluid, rotating waves, instability, bifurcations

**Author for correspondence:**

Sebastian A. Altmeyer

e-mail: [sebastian.andreas.altmeyer@upc.edu](mailto:sebastian.andreas.altmeyer@upc.edu)

Electronic supplementary material is available online at <https://doi.org/10.6084/m9.figshare.c.6412326>.

# Arrow-shaped elasto-inertial rotating waves

Jose M. Lopez<sup>1,2</sup> and Sebastian A. Altmeyer<sup>1</sup>

<sup>1</sup>Department of Fisica Aplicada, Universitat Politècnica de Catalunya, Girona s/n, Modul B4 Campus Nord, 08034 Barcelona, Spain

<sup>2</sup>Universidad de Málaga, Campus de Teatinos, s/n, 29071, Málaga, Spain

SAA, 0000-0001-5964-0203

We present direct numerical simulations of the Taylor–Couette flow of a dilute polymer solution when only the inner cylinder rotates and the curvature of the system is moderate ( $\eta = 0.77$ ). The finitely extensible nonlinear elastic–Peterlin closure is used to model the polymer dynamics. The simulations have revealed the existence of a novel elasto-inertial rotating wave characterized by arrow-shaped structures of the polymer stretch field aligned with the streamwise direction. This rotating wave pattern is comprehensively characterized, including an analysis of its dependence on the dimensionless Reynolds and Weissenberg numbers. Other flow states having arrow-shaped structures coexisting with other types of structures have also been identified for the first time in this study and are briefly discussed.

This article is part of the theme issue 'Taylor–Couette and related flows on the centennial of Taylor's seminal *Philosophical Transactions* paper (Part 2)'.

## 1. Introduction

In the century that has elapsed since the pioneering work of Taylor [1], the Taylor–Couette flow (TCF), i.e. the fluid flow contained in the annular gap between two vertical concentric cylinders, has become one of the most prominent models for investigating flow pattern formation, instabilities and turbulence in rotating shear flows [2–5]. This popularity has been partly motivated by the fact that, in many configurations of this system, the transition to the turbulence is supercritical, i.e. it occurs through a well-defined sequence of linear instabilities to flow patterns of increasing spatio-temporal complexity eventually leading to turbulence. The specific characteristics of these flow patterns depend crucially on the geometry of the apparatus (the curvature

and the length-to-gap aspect ratio), the container boundaries and the relative rotation of the cylinders. However, it is frequently observed that the transition from axisymmetric to three-dimensional flow gives rise to waves that propagate in the azimuthal direction while keeping a constant shape. These flow states are known as rotating waves and appear when the system undergoes a Hopf bifurcation that breaks its  $\text{SO}(2)$  symmetry. The best-known example of a rotating wave pattern is the so-called wavy vortex flow, which emerges from the Taylor vortices as the inner cylinder rotation speed increases for a wide range of curvatures and aspect ratios [6–11]. Another well-studied example of rotating waves in pure hydrodynamic TCF is the ribbons (RB) pattern, which emerges when the cylinders counter-rotate [5].

While TCF has traditionally been studied using Newtonian fluids, a growing interest has been shown recently in investigating non-Newtonian cases, especially when the working fluid is a dilute polymer solution. Due to their viscoelastic properties, long-chain polymers (even in small amounts) may substantially change the stability and spatio-temporal characteristics of the flow with respect to those in the Newtonian case. First observations of such a phenomenon date back about 30 years, with the detection of flow instability in the absence of inertia [12–14]. These studies were followed by a number of experimental works that explored in detail the formation of flow patterns depending on the relative importance between inertial and elastic effects [15–19]. A wide range of flow patterns was discovered, in many cases coexisting for the same values of the control parameters (the Reynolds and Weissenberg numbers), and it was concluded that observing one or more flow states was highly sensitive to polymer properties, initial conditions and experimental protocol. One of the most typical states reported in these studies was the RB pattern, a rotating wave formed by two (symmetry degenerated) spiral waves that propagate axially in opposite senses [15,16]. As for Newtonian cases, viscoelastic RB arise from a supercritical Hopf bifurcation of the circular Couette flow (CCF), but unlike Newtonian fluids, it is not necessary that the cylinders counter-rotate (they are observed even in the classical setup, where only the inner cylinder rotates). Depending on the flow's elasticity, they may occur at rotation speeds one order of magnitude smaller than those at which rotating waves exist in isothermal Newtonian TCF, and they have been found to play a major role in several transition routes to elasto-inertial turbulence (EIT) [20–25]. Other coherent states which are frequently encountered in experiments on TCF of a dilute polymer solution are diwhirls (DW), oscillatory strips (OS), disordered oscillations (DO) or flames (FL) [15–19]. However, unlike RB, the transition to these flow states, which may occur either from CCF or RB, is abrupt and highly hysteretic.

These coherent states could not be replicated in simulations until the late 2000s [26,27]. The use of the FENE-P (finite extensibility nonlinear elastic-Peterlin) closure was critical to the success of these simulations because it included important effects of the polymer's finite extensibility that had been previously overlooked in numerical works. In addition to demonstrating the ability of the FENE-P model to accurately simulate polymer dynamics, the authors detailed the spatio-temporal characteristics of the flow states they discovered. However, because the parameter space was not thoroughly explored, there could be many more coherent states than those reported in these studies. Since then, there has been a growing interest in studies aimed at characterizing EIT [28–30] and no further studies (both numerical and experimental) on flow pattern formation and transition to the EIT have been performed until very recently [20,31–35]. Given the problem's large parameter space, the large number of states that can coexist for the same values of the control parameters, and the scarcity of numerical studies on viscoelastic flow patterns, it is reasonable to expect previously unreported states to emerge in numerical studies on these flows.

Whereas for TCF, coherent elasto-inertial flow patterns have been studied for nearly three decades, for parallel shear flows, the first coherent viscoelastic structure has only recently been found in simulations of a two-dimensional channel flow [36,37]. These structures are travelling waves (the analogue of the rotating waves in parallel flows) that propagate downstream at a speed close to the centreline velocity. The hallmark of these viscoelastic travelling waves is the existence of arrowhead structures in the polymer stretch field which are oriented in the

streamwise direction. It has been speculated that these structures may be caused by an increase in the elongational viscosity of the fluid due to polymer stretching in the flow direction [37]. This characteristic suggests that these arrow-shaped structures of polymer stretch may not be exclusive to parallel shear flows, but a universal feature of flow systems where polymers are subjected to elongational flow. In TCF, for instance, polymers are stretched by the primary flow in the azimuthal direction. Hence, an increase in the fluid's elongational viscosity might result in arrow-shaped structures aligned with the azimuthal direction. However, as far as we are aware, no evidence of these structures in flows with curved streamlines has been reported yet.

In this paper, using direct numerical simulations of the TCF of a dilute polymer solution, where the FENE-P closure is used to model the polymer dynamics, we show that arrow-shaped structures of polymer stretch aligned with the streamwise direction (in this case the azimuthal direction) also exist in TCF. These structures are identified in elasto-inertial rotating waves that propagate with a very slow frequency and in chaotic states. We determine the range of existence of the rotating wave solutions in the parameter space defined by the dimensionless Reynolds and Weissenberg numbers and show how the characteristics of the arrow-shaped structures change as these parameters are varied. We also briefly discuss other solution branches found in our study.

## 2. Problem formulation and methodology

### (a) Governing equations and dimensionless parameters

We consider the flow of a dilute polymer solution driven in the annular gap between two vertical, rigid, and independently rotating cylinders of height  $h$ . The inner cylinder of radius  $r_i$  rotates at angular speed  $\Omega_i$  and the outer cylinder of radius  $r_o$  is kept at rest, i.e.  $\Omega_o = 0$ . The fluid is incompressible and the dynamics is governed by the Navier–Stokes and continuity equations. An additional equation is needed to describe the temporal evolution of a polymer conformation tensor,  $\mathbf{C}$ , which contains the ensemble average elongation and orientation of all polymer molecules in the flow. Each polymer molecule is modelled by a finitely extensible elastic dumbbell [38]. The dimensionless equations read

$$\left. \begin{aligned} \nabla \cdot \mathbf{v} &= 0, \\ \partial_t \mathbf{v} + \mathbf{v} \cdot \nabla \mathbf{v} &= -\nabla P + \frac{\beta}{Re} \nabla^2 \mathbf{v} + \frac{(1-\beta)}{Re} \nabla \cdot \mathbf{T} \\ \partial_t \mathbf{C} + \mathbf{v} \cdot \nabla \mathbf{C} &= \mathbf{C} \nabla \mathbf{v} + (\nabla \mathbf{v})^T \mathbf{C} - \mathbf{T}, \end{aligned} \right\} \quad (2.1)$$

and

where  $\mathbf{v} = (u, v, w)$  is the velocity vector field in cylindrical coordinates  $(r, \theta, z)$ ,  $P$  is the pressure,  $\beta = \nu_s/\nu$  indicates the relative importance between the solvent viscosity,  $\nu_s$ , and the viscosity of the solution at zero shear rate,  $\nu$ . The length scale of the system is normalized with the gap width,  $d = r_o - r_i$ , the velocity with the inner cylinder velocity,  $\Omega_i r_i$ , the pressure with the dynamic pressure,  $\rho(\Omega_i r_i)^2$ , where  $\rho$  is the fluid's density and the polymer conformation tensor with  $k_B T_e / H$ , where  $k_B$  denotes the Boltzmann constant,  $T_e$  is the absolute temperature and  $H$  is the spring constant.

The coupling between the polymers and the Navier–Stokes equations is realized through the polymer stress tensor  $\mathbf{T}$ , which is calculated using the FENE-P model [38],

$$\mathbf{T} = \frac{1}{Wi} \left( \frac{\mathbf{C}}{1 - (tr(\mathbf{C})/L^2)} - \mathbf{I} \right), \quad (2.2)$$

where  $\mathbf{I}$  is the unit tensor,  $tr(\mathbf{C})$  is the trace of the polymer conformation tensor,  $L$  denotes the maximum polymer extension parameter and  $Wi$  is the Weissenberg number (defined below).

Periodic boundary conditions are imposed in the  $z$ - and  $\theta$ -directions, whereas the boundary conditions at the cylinders are

$$\mathbf{v}(r_i, \theta, z) = (0, 1, 0) \quad \text{and} \quad \mathbf{v}(r_o, \theta, z) = (0, 0, 0). \quad (2.3)$$

The system is governed by the following independent non-dimensional parameters:

$$\left. \begin{array}{l} \text{Reynolds number: } Re = \frac{\Omega_i r_i d}{\nu}, \\ \text{Weissenberg number: } Wi = \frac{\lambda}{[d/(\Omega_i r_i)]} \\ \text{Radius ratio: } \eta = \frac{r_i}{r_o} \\ \text{Aspect ratio: } \Gamma = \frac{h}{d}, \end{array} \right\} \quad (2.4)$$

and

where  $\lambda$  is the polymer relaxation time and  $d/(\Omega_i r_i)$  is the advective time scale.

In this paper, the radius ratio and aspect ratio are fixed to  $\eta = 0.77$  and  $\Gamma = 2\pi$ , respectively. A constant polymer concentration  $\beta = 0.871$  is used and the maximum polymer extension parameter  $L$  is set to 100, in accordance with recent studies of EIT on viscoelastic TCF [28,29,34,39]. The flow's elasticity level, quantified by the elasticity number  $El = Re/Wi$ , ranges from 0.01 to 1. The parameter space is explored by either fixing  $Re$  and varying  $Wi$  or vice versa, and consequently, the value of  $El$  changes among simulations. This protocol differs from that in [26,27], the only numerical study on flow pattern formation in viscoelastic TCF conducted to date, where the simulations were performed at a constant  $El$  for five different  $El$  values ( $El = 0.33$ ,  $El = 0.50$ ,  $El = 0.75$ ,  $El = 1$  and  $El = 30$ ). Another difference with respect to this study is the polymer concentration. The polymer solution used in our simulations is nearly 10% more diluted than that used in [26,27] ( $\beta = 0.8$  in these references).

## (b) Numerical methods

The governing equations (2.1) are solved with the open source code nsCouette [40]. The code is a combination of high-order central finite differences on a Gauss–Lobatto–Chebyshev grid in  $r$  and Fourier–Galerkin expansions in  $z$  and  $\theta$ . Decoupling between pressure and velocity field is realized by a pressure Poisson equation formulation. The free divergence condition is enforced by using an influence matrix technique, so that this condition is satisfied up to machine error. A second-order accurate predictor–corrector scheme based on the Crank–Nicolson method is used to carry out the time integration (see [41,42] for further details about the timestepper). Following the customary approach in numerical simulations of viscoelastic flows using pseudo-spectral codes, a small amount of artificial diffusion is added to stabilize the integration. The reason to include this diffusion is the hyperbolic nature of the time evolution equation for  $\mathbf{C}$ . In the absence of diffusion, integration of this equation often results in an accumulation of numerical error, which in many cases produce numerical breakdown. This issue can be overcome by adding a Laplacian term,  $(1/ReS_c)\nabla^2\mathbf{C}$ , to the right-hand side of this hyperbolic equation, where the Schmidt number,  $S_c = \nu/\kappa$ , quantifies the ratio between the viscous and artificial diffusivities. In the simulations presented here,  $S_c$  has been varied between 50 and 100, so that the artificial diffusion coefficient,  $1/ReS_c$ , is of the order of  $10^{-4}$ . Several tests using larger  $S_c$  values ( $S_c$  up to 200 were tested) have been conducted to verify that further reduction in the diffusion coefficient does not alter significantly the results of the simulations. The number of radial nodes and Fourier modes used in the computations were  $m_r = 64$ ,  $m_\theta = 33$  and  $m_z = 256$ , whereas the time step size was set to  $5 \times 10^{-3}$ .

## 3. Arrow-shaped structures of polymer stretch

To probe whether arrow-shaped structures of polymer stretch exist in viscoelastic TCF, we have conducted simulations at low  $Re$  values ( $Re \leq 100$ ) while keeping  $Wi = 15$ . The elasticity number,  $El = Wi/Re$ , in these simulations falls within the range  $0.15 \leq El \leq 0.75$ , which is consistent with the elasticity levels at which arrowhead structures have been observed in channels. The simulations were started from the laminar state, previously computed, which was perturbed by

a disturbance of the form,

$$u = A(r - r_i)(r - r_o)\cos(\theta + kz) \quad (3.1)$$

and

$$w = -A \frac{(r - r_i)(r - r_o)}{r} (5r^2 - 3(r_i + r_o)r + r_i r_o) \frac{\sin(\theta + kz)}{k}, \quad (3.2)$$

where  $k$  is the axial wavenumber and  $A$  denotes the amplitude of the perturbation. If the value of  $A$  is sufficiently large, the simulations converge to a rotating wave with azimuthal wavenumber  $m = 1$ . The amplitude threshold required to cause the instability is small (it can be as small as  $A \sim O(10^{-8})$  at the largest  $Re$  investigated), yet below this threshold the energy of the perturbation decays and the laminar state persists. This indicates that these rotating wave patterns are driven by nonlinear effects. We note that the existence of subcritical instabilities triggered by very low amplitude thresholds is consistent with recent findings in other studies on viscoelastic flows at low Reynolds numbers [43,44]. Depending on the value of  $k$  used in the initial condition, flow patterns with three or four pairs of counter-rotating vortices were obtained. In the following, we will restrict the discussion to the case where the flow pattern has four vortex pairs.

The upper panels of figure 1 show colour maps of the trace of the polymer conformation tensor,  $tr(\mathbf{C})$ , normalized with the maximum elongation of the polymers,  $L^2$ , in a cylindrical section  $(\theta, z)$  at three different radial locations (indicated on top of each panel) for a simulation conducted at  $Re = 90$ . This quantity indicates the degree of stretching of the polymer chains. High values of  $tr(\mathbf{C})/L^2$  (dark regions) denote highly stretched polymers, whereas low values of  $tr(\mathbf{C})/L^2$  (lighter regions) indicate that polymers are weakly stretched. As is evident from the figure, the most distinctive feature of this flow state is the existence of regions of highly stretched polymers in the shape of an arrow. Due to this characteristic, it will be hereafter referred to as arrow-shaped rotating wave (ArrowRW). These arrow-shaped structures are observed across the radial gap, except for the regions very close to the cylinders, but their shapes differ depending on the radial location. As one moves from the outer to the inner cylinder (from right to left in the figure), the body of the arrow progressively shortens and the axial extent of the arrowhead increases.

To illustrate the correspondence between polymer stretch and flow velocity, the lower panels of figure 1 show colour maps of the radial velocity in the same section and at the same time instant as the upper panels. Positive velocity (red areas) denotes fluid motion from the inner to the outer cylinder, i.e. outflows, whereas negative velocity (blue areas) indicates fluid moving from the outer to the inner cylinder, i.e. inflows. When the upper and lower rows of the figure are compared, it becomes evident that the arrow-shaped structures of highly stretched polymers are associated with inflow regions, whereas outflows occur in areas where the polymer stretch is lower (less than 25% of  $L^2$ ). The wake of the arrows, on the other hand, corresponds to the vicinity of the boundaries between inflows and outflows, where the radial velocity is close to zero. As seen, the velocity in the inflows is higher than that of the outflows. This characteristic is caused by the elastic force created by the stretched polymers. This force acts radially inward and hence enhances fluid motion through the inflows while slowing down the motion through the outflows. This creates an asymmetry between inflows and outflows (the axial extent of the outflows is larger than that of the inflows) which has been discussed in detail in [34,45]. The highest degree of asymmetry occurs near the outer cylinder, where the elastic force exhibits strong localized peaks that result in strong localized inflow jets (note that the axial extent of the outflow regions here is more than twice that of the inflow regions, see panel corresponding to  $r - r_i = 0.75$ ). However, as we move towards the inner cylinder, the magnitude of the elastic force decays gradually, and consequently, the degree of asymmetry between inflows and outflows also diminishes (see panels for  $r - r_i = 0.50$  and  $r - r_i = 0.25$ ). The changes observed in the arrow-shaped structures when these are plotted at distinct radial locations (upper panels) can thus be ascribed to the radial dependence of the elastic force and how this modifies the axial extent of the inward motion.

To provide a simpler quantitative characterization of the polymer stretch, we show in figure 2 the variation of  $tr(\mathbf{C})/L^2$  along the azimuthal direction at fixed radial (mid-gap) and axial ( $z = 2.25$ )

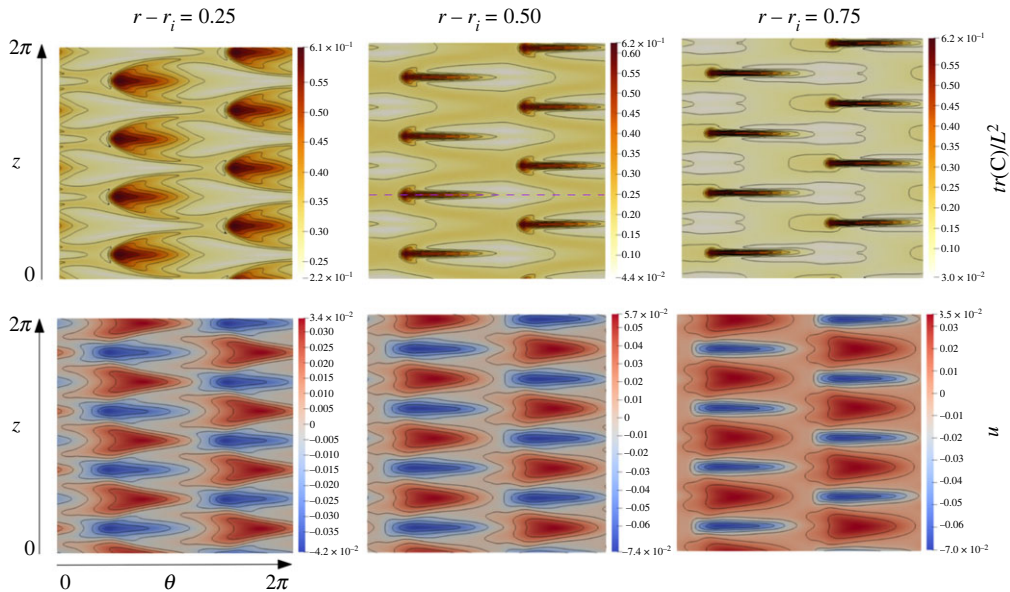


**Figure 1.** The upper panels show colour maps of the trace of the polymer conformation tensor,  $tr(C)$ , normalized with the maximum polymer extension,  $L^2$ , in cylindrical sections  $(\theta, z)$  at three different radial locations. Dark (light) regions indicate regions where polymers are highly (slightly) stretched. The lower panels display colour maps of the radial velocity,  $u$ , at the same time instant and in the same cylindrical sections as the upper panels. Red (blue) areas indicate outflows (inflows). The example shown corresponds to a snapshot of a simulation with  $Re = 90$ ,  $L = 100$ ,  $\beta = 0.871$  and  $Wi = 15$ . Eight contours evenly spaced across the entire range of values (indicated in the colourbar) are shown in each case. The flow direction is from left to right. (Online version in colour.)

locations for the same snapshot shown in figure 1 (i.e. along the purple dashed line shown in that figure). We note that the same plot is obtained if  $tr(C)/L^2$  is plotted as a function time at a fixed azimuthal location (time is shown in the upper abscissa of the figure). This happens because in rotating waves the variation in  $\theta$  is commensurate with the temporal evolution of the flow pattern. Figure 2 shows that the emergence of the arrow-shaped structures is associated with an abrupt local increase of  $tr(C)/L^2$ . The maximum value of  $tr(C)/L^2$  is achieved in the head of the arrow, shortly after the sudden increase takes place, and it can be as large as 0.75 (i.e. 75% of the maximum polymer elongation) for the largest values of  $Re$  and  $Wi$  simulated in this study. The decay of  $tr(C)/L^2$  exhibits two phases: a slow decay that coincides with the body of the arrow and a sharper decay that occurs in the wake behind the arrow ( $2 < \theta < 3.5$ ). The minimum value of  $tr(C)/L^2$  is reached in the latter region and it is in all simulations lower than 10% of the maximum polymer elongation. After the minimum,  $tr(C)/L^2$  increases gradually until it reaches a value of nearly 0.2 which remains constant before the emergence of the arrow-shaped structure.

We finally show in figure 3 the radial dependence of the polymer stretch (upper row) and flow streamlines (lower row) as a function of  $\theta$ . The values of  $\theta$  at which snapshots are displayed are shown as dashed lines in figure 2. The leftmost panels (A,  $\theta = 0.25$ ) illustrate the flow upstream of the arrow-shaped structure, far from the arrowhead. Polymers here are more stretched in the region near the inner cylinder. This circumstance appears to be related to the emergence of flow recirculation zones near the inner cylinder (see the leftmost panel of the lower row), which displace the main vortices towards the outer cylinder. As the arrowhead is approached, the intensity of the vortices increases and the recirculating vortices near the inner cylinder weaken. As a result, polymers get increasingly more stretched near the outer cylinder (see panels B, for  $\theta = 0.5$ ). Jets of highly stretched polymers emanate then from the outer cylinder and move towards

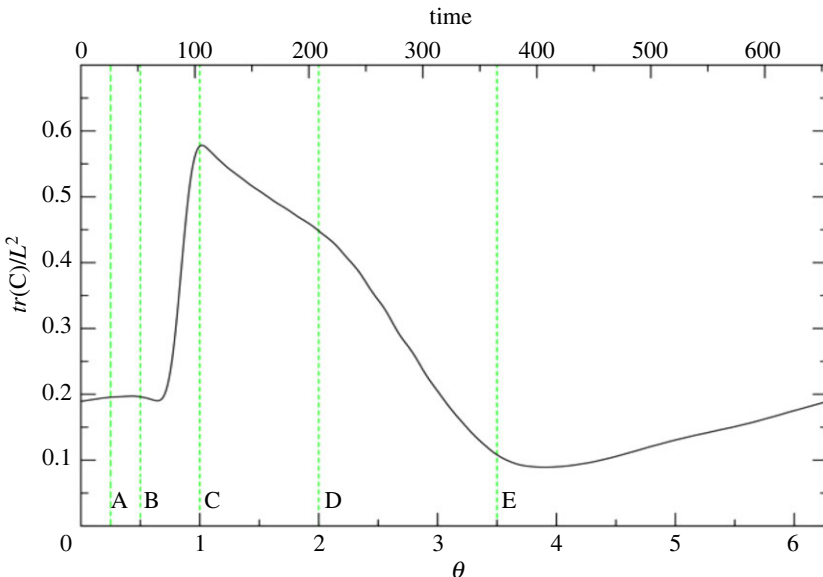


**Figure 2.** Trace of the polymer conformation tensor, normalized by  $L^2$ , obtained at the mid-gap ( $r - r_i = 0.5$ ) and  $z/d = 2.25$  as a function of  $\theta$  (lower abscissa) and time (upper abscissa). The values of  $\theta$  for which meridional sections are shown in figure 3 are represented as green dashed lines. (Online version in colour.)

the inner cylinder through the inflows (see panels C, which corresponds to the arrowhead,  $\theta = 1$ ). Vigorous counter-rotating vortex pairs, with a clear asymmetry between inflows and outflows, as described above, extend across the entire radial gap (lower C panel). This situation continues as one moves toward the bottom end of the arrow-shaped structure. When the jet of highly stretched polymers meets the inner cylinder, it begins to spread along the wall (see panel D, for  $\theta = 2$ ), and polymers get progressively more stretched in this region. The initial situation where the recirculation zones appear near the inner cylinder and the vortices move towards the outer cylinder is eventually recovered (see panel E, for  $\theta = 3.5$ ) and the cycle starts again (with the vortices and regions of highly stretched polymers shifted by half a wavelength with respect to the first half of the rotation period).

#### 4. *Re* and *Wi* parameter dependence

To establish the range of existence of the ArrowRW solution in the *Wi-Re* parameter space and how the characteristics of the arrow-shaped structures change with varying these parameters, we have conducted natural continuation of this flow state. The black line in figure 4a shows the deviation of the volume averaged kinetic energy,  $k_e$ , with respect to its laminar value, for the ArrowRW state at the *Re* values at which this solution is found when *Wi* = 15. We note that for this *Wi* value, the base flow is linearly stable. The ArrowRW solution vanishes at a saddle-node bifurcation that takes place at  $Re \approx 20$ . It should be noted that this value of *Re* is well below that at which Taylor vortices appear in the Newtonian case ( $Re \approx 90$ ), clearly showing that the instability relies on the interplay between inertia and elasticity. The lower branch solution that continues at lower energy towards larger *Re* values is unstable, but it could be detected by using the bisection method introduced by Itano & Toh [46] (see black dashed line in figure 4a). Only a few points of this solution branch have been computed, as flow states here are characterized by very weakly stretched polymers and arrow-shaped structures are no longer observed. To follow the ArrowRW solution branch near the saddle-node, it is necessary to vary *Re* in very small steps. If the change in *Re* is too large, the simulations converge to a different flow state, labelled LArrowRW in the figure,

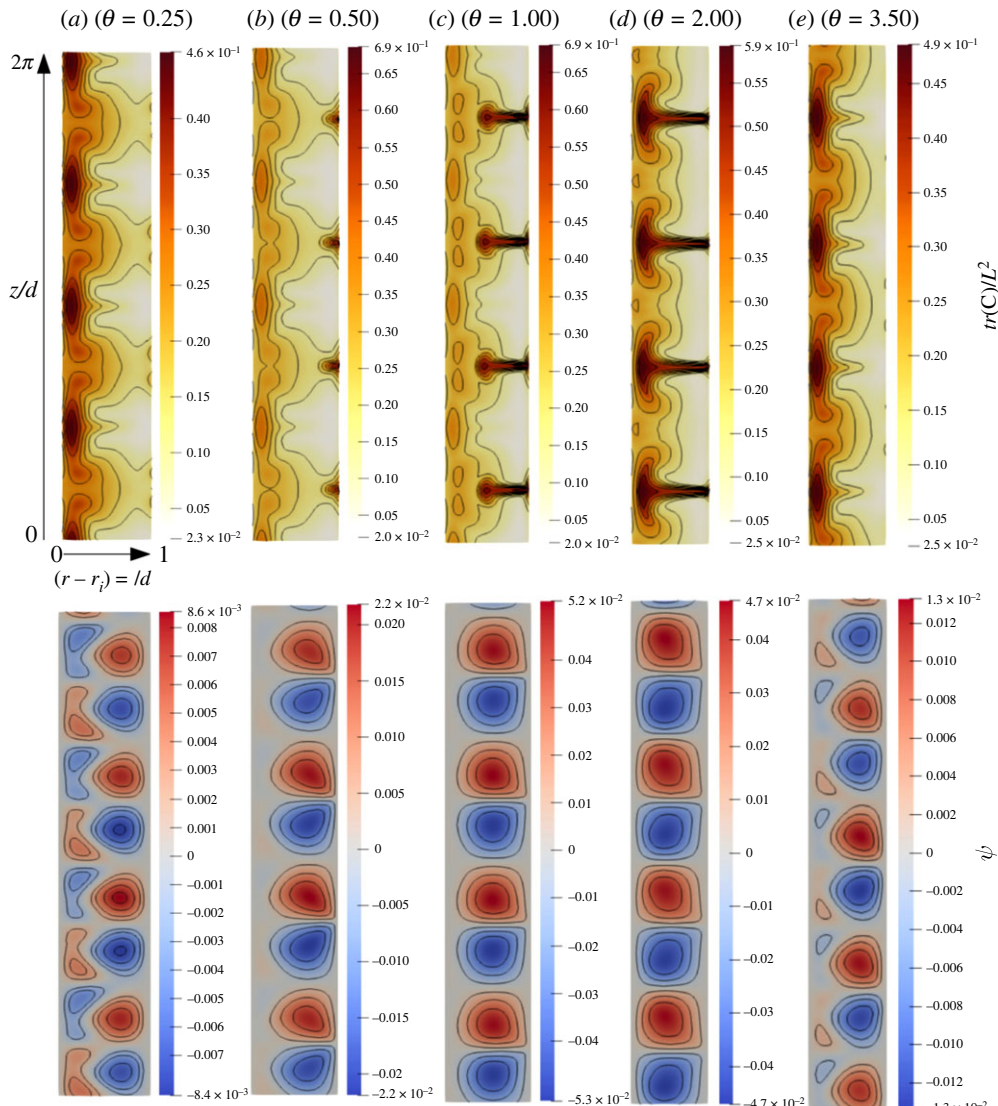


**Figure 3.** Colour maps of polymer stretch (upper row) and flow streamlines  $\psi$  (lower row) shown in meridional sections ( $r, z$ ) obtained at the values of  $\theta$  indicated at the top of each panel (and shown as dashed (green) lines in the figure 1). Eight contours evenly spaced across the full range of values have been added to each panel. (Online version in colour.)

which is characterized by azimuthally localized arrow-shaped structures (this state is illustrated in figure 7c and described in more detail in §5). The LArrowRW coexists with the ArrowRW for  $20 \lesssim Re \lesssim 45$ , and it could be followed up to  $Re \approx 16.5$ , a value slightly lower than that at which the ArrowRW disappears. Below this threshold, the flow lamina rises.

The highest  $Re$  value at which the ArrowRW exists for  $Wi = 15$  is  $Re = 100$ . With further increase in  $Re$ , the flow pattern begins to exhibit additional modulations and complex spatio temporal dynamics set in. These states are, however, outside the scope of this paper and will be discussed elsewhere. As expected, polymer stretch increases with increasing  $Re$  due to the increase in the magnitude of the mean azimuthal velocity, reaching a maximum value of 75% of  $L^2$  for  $Re = 100$ . The upper row of figure 5 shows colour maps of the polymer stretch in a cylindrical section at the mid-gap for the simulations performed at  $Re = 25$  and  $Re = 50$ . Along with the middle panel in the upper row of figure 1, for  $Re = 90$ , these figures illustrate the variation

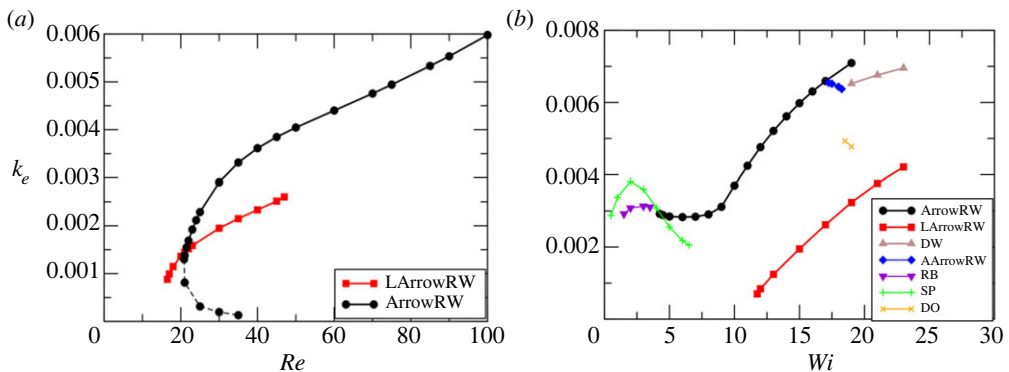


**Figure 4.** Variation of the deviation of the volume average kinetic energy in the flow states found in the present study as the  $Re$  and  $Wi$  numbers are varied. Note that the volume average kinetic energy corresponding to the laminar state has been subtracted. (a)  $Re$  number dependence when  $Wi = 15$  and (b)  $Wi$  number dependence when  $Re = 100$ , except for the LArrowRW state where  $Re = 30$ . The acronyms shown in the legend stand for: arrow-shaped rotating wave (ArrowRW), localized arrow-shaped rotating wave (LAarrowRW), asymmetric arrow-shaped rotating wave (AAarrowRW), spirals (SP), diwhirls (DW), ribbons (RB) and disordered oscillations (DO). (Online version in colour.)

of the structures of polymer stretch as the  $Re$  number increases along the upper branch solution while holding the  $Wi$  number constant. For  $Re$  values near the saddle-node bifurcation (see panel for  $Re = 25$ ), the arrow-shaped structures are not yet evident. The maximum polymer stretch here is still rather moderate (less than 50% of the maximum polymer extension) and this results in oval-shaped structures, where the azimuthal extent is only slightly larger than the axial extent (see darker zones). As  $Re$  increases and the stretching of the polymers increases, the structures become increasingly more elongated in the azimuthal direction and the arrow shape emerges. The right upper panel of figure 5 shows that for  $Re = 50$ , the arrow-shaped structures can already be clearly distinguished, even though the highest polymer stretch is still not too large (only slightly above half of  $L^2$ ).

The black line in figure 4b illustrates the variation of the ArrowRW state when  $Re = 100$  and  $Wi$  is varied. The minimum  $Wi$  number at which the solution could be followed is  $Wi = 4.25$ . Below this threshold, the ArrowRW becomes unstable and simulations converge to either RB or Spirals (SP). Two distinct trends are observed in the energy of the ArrowRW. It remains nearly constant when  $4.25 \leq Wi \leq 9$  and increases with increasing  $Wi$  when  $Wi > 9$ . Despite the transition between the two regimes appearing to be rather smooth, the flow structures are qualitatively and quantitatively very different. Whereas for large  $Wi$  numbers, the arrow-shaped structures of highly stretched polymers shown in figure 1 are observed, in the regime where the energy is almost constant, the structures of polymer stretch take the form of a fork oriented in the flow direction (see left panel of figure 5 for  $Wi = 6$ ). Interestingly, the amount of polymer stretch in these structures is surprisingly low (below 10% of  $L^2$ ). It must be noted that the simulation for  $Wi = 4.25$  was run for nearly 10 000 advective time units. The solution persisted for this time and there was not any sign that there could be a change in the flow pattern with further simulation time. Hence, this surprising solution appears to be stable. As  $Wi$  increases, the forked-shaped structures are gradually replaced by arrow-shaped structures. The lower right panel shows the structures for the simulation conducted at  $Wi = 9$ , which marks the transition between the regimes of constant and increasing energy. As seen, arrow-shaped structures of moderately stretched polymers can already be identified at this  $Wi$  value. The largest  $Wi$  at which the ArrowRW state was found is  $Wi = 19$ . Above this value, the solution becomes unstable and the simulations converge to a stationary pattern of elastically induced vortices known as DW (brown line in figure 4b). The dynamics of the DW have been recently shown in detail in [34] and thus will not be discussed here. Other solution branches, labelled as AArrowRW and DO in the figure, were also found at large  $Wi$  numbers and will be discussed in §5.

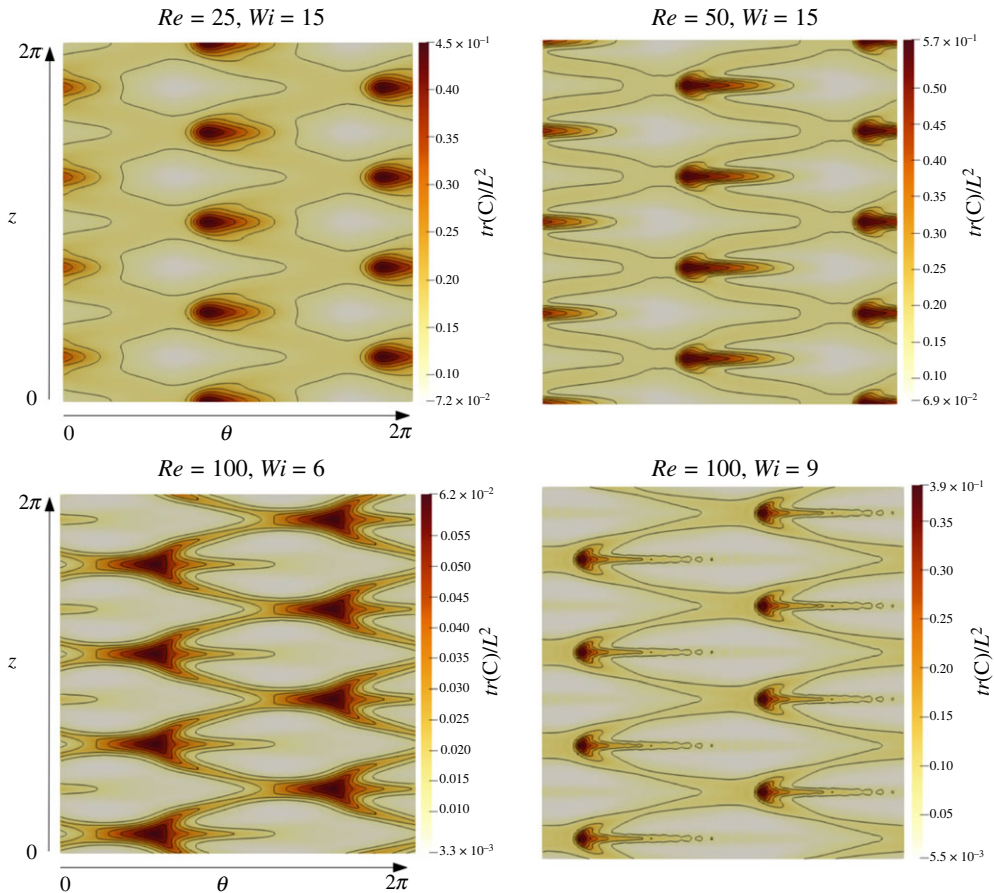


**Figure 5.** Variation of the structures of polymer stretch as the  $Re$  (upper row) and  $Wi$  (lower) numbers are varied. Cylindrical sections ( $\theta, z$ ) obtained at the mid-gap are shown. Eight contours evenly spaced across the full range of values have been added to each panel. (Online version in colour.)

All the arrow-shaped rotating waves found in this study propagate very slowly, with a rotation frequency (calculated from fast Fourier transform of a time series of the radial velocity) of the order of  $f \sim 10^{-3}(\Omega_i r_i)/d$ . Moreover, it is observed that the rotation frequency decreases as  $Re$  or  $Wi$  increases.

We finally investigate the relationship between the changes observed in the volume averaged kinetic energy as  $Re$  and  $Wi$  are varied and the physical mechanisms governing the physics of this problem (i.e. inertial, viscous and elastic effects). To that extent, we have calculated the inertial ( $\mathcal{P}$ ), viscous ( $\epsilon$ ) and polymeric ( $\Pi_e$ ) contributions to the integral energy balance of the ArrowRW solution. For viscoelastic flows, the integral energy balance reads [47],

$$\int_V \mathcal{P} dV - \int_V \epsilon dV - \int_V \Pi_e dV = 0, \quad (4.1)$$

and  $\mathcal{P}$ ,  $\epsilon$  and  $\Pi_e$  are calculated as

$$\mathcal{P} = -\overline{u'v'} \frac{\partial \bar{v}}{\partial r} + \overline{u'v'} \frac{\bar{v}}{r}, \quad (4.2)$$

$$\epsilon = \frac{2\beta}{Re} \overline{S' : S'}, \quad (4.3)$$

$$\Pi_e = \frac{1-\beta}{Re} \overline{S' : T'}. \quad (4.4)$$

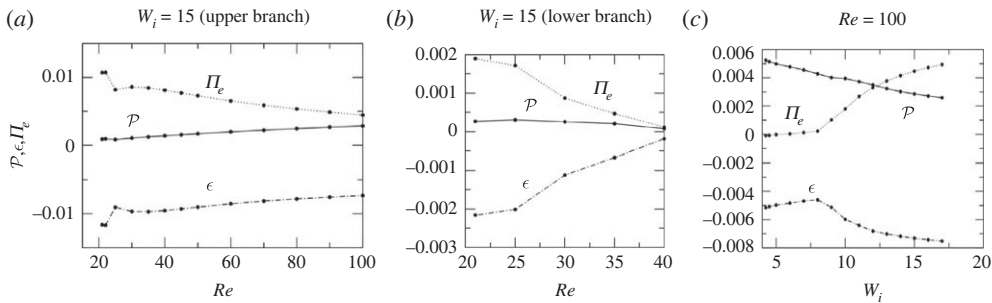


**Figure 6.** Variation of the inertial ( $\mathcal{P}$ ), viscous ( $\epsilon$ ) and polymeric ( $\Pi_e$ ) contributions to the integral energy balance (i.e. kinetic energy budgets) in (a) upper branch solution of the ArrowRW for  $W_i = 15$ , (b) lower branch solution of the ArrowRW for  $W_i = 15$  and (c) ArrowRW for  $Re = 100$  and varying  $W_i$ . In each panel,  $\mathcal{P}$ ,  $\epsilon$  and  $\Pi_e$  are shown as solid, dash-dotted and dotted lines, respectively. (Online version in colour.)

Here, the overline denotes mean quantities,  $S' = (\nabla \mathbf{v}' + \nabla \mathbf{v}'^T)/2$  indicates the rate of strain tensor and the prime symbol denotes deviations of the velocity or polymer stress tensor from their mean values. It must be noted that  $\mathcal{P}$  and  $\epsilon$  always act as a source and a sink of energy, respectively. However,  $\Pi_e$  can be either a source or a sink depending on whether the sign of the integral is negative or positive (note that there is a minus sign in front of the integral). In figure 6a, it is shown how the values of these three integrals (including the sign in front of them) vary with  $Re$  along the upper branch solution curve. As seen, for all  $Re$  numbers, the polymeric contribution is the dominant energy source (polymers are injecting energy into the flow), reflecting again the elastic nature of the ArrowRW solution. At the lowest values of  $Re$  (near the turning point), the contribution of  $\Pi_e$  is larger than that of  $\mathcal{P}$  by two orders of magnitude. However, as  $Re$  increases, the contribution of  $\mathcal{P}$  increases and the contribution of  $\Pi_e$  decreases, so that at the largest  $Re$  values where the ArrowRW solution exists, they are similar in magnitude. This behaviour was expected, as in this analysis we keep  $W_i = 15$ , and so, as  $Re$  increases, the relative importance of inertial effects against elastic effects increases. In figure 6b, the variation of the contributions of  $\mathcal{P}$ ,  $\epsilon$  and  $\Pi_e$  is shown for the lower branch solution curve when  $W_i = 15$ . While the contribution of  $\Pi_e$  continues to be the dominant energy source near the turning point, its magnitude decays fast as  $Re$  increases and it becomes of the same order of magnitude as the inertial contribution at  $Re \approx 30$ . These analyses show that, at this  $Wi$  value, steady ArrowRW states appear only when the flow is entirely dominated by elasticity, and that these solutions become unstable as the inertial effects become comparable to elastic effects. Finally, figure 6c illustrates the same analysis for the case in which  $Re = 100$  and  $W_i$  is varied. It is observed that, at low  $Wi$  numbers, inertia is the dominant energy source. Although the net polymeric contribution at these  $Wi$  is positive and hence polymers also act as an energy source, its magnitude is very small when compared to the inertial contribution. Interestingly, this low contribution of the polymers to the integral energy balance persists until  $Wi \approx 9$  is achieved, and it is thus consistent with the regime where the volume averaged kinetic energy is constant and stable forked-like structures are observed. Beyond this threshold, the contribution of  $\Pi_e$  grows quickly with increasing  $Wi$ , and this, along with the gradual decrease in the inertial contribution, results in a flow regime similar to that described in figure 6a, where the polymeric contribution is the main energy source. It is when this happens that arrow-shaped structures of highly stretched polymers are observed.

## 5. Other solution branches

Having presented the ArrowRW solution in detail, we next focus on other solution branches where arrow-shaped structures of polymer stretch are also present. The first of these solutions, which has been dubbed asymmetric arrow rotating wave (AArrowRW), emerges at  $Wi \approx 17.3$  (for  $Re = 100$ ) when the ArrowRW undergoes a symmetry-breaking bifurcation that breaks the axial

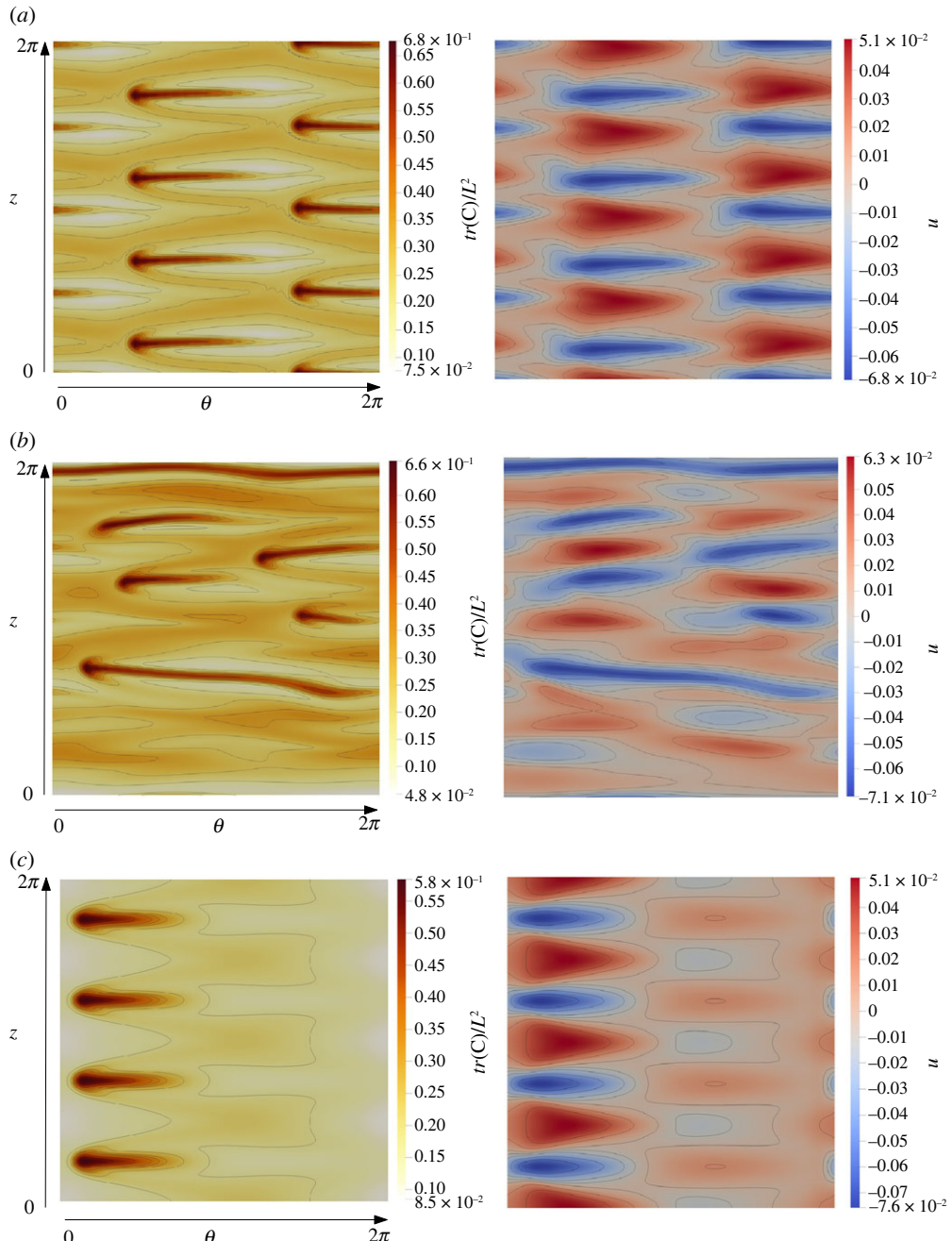


**Figure 7.** Colour maps of the polymer stretch field (left panels) and radial velocity (right panels) illustrating other flow states where arrow-shaped structures of polymer stretch are also observed. (a) AArrowRW for  $Re = 100$  and  $Wi = 18$ , (b) D0 for  $Re = 100$  and  $Wi = 20$  and (c) LArrowRW for  $Re = 30$ , and  $Wi = 15$ . As in the previous figures, a cylindrical section ( $\theta, z$ ) obtained at the mid-gap is shown in each panel. Eight contours evenly spaced across the entire range of values (indicated in the colourbar) are shown in each case. The flow direction is from left to right. (Online version in colour.)

symmetry of the structures. This characteristic becomes clear when figure 7a, which illustrates the AArrowRW state at  $Re = 100$  and  $Wi = 18$ , is compared with figure 1 (middle panels). Whereas for the ArrowRW, the arrow-shaped structures (including the wake) are symmetric with respect to the horizontal plane passing through the axis of the arrow, this symmetry is not preserved by the

AArrowRW. In this latter state, there is an increase of the polymer stretch in the lower half of the structures (see that the colour intensity in this region right after the arrowhead is slightly darker than in the upper half), which results in the wake extending over a larger azimuthal distance than in the upper half. This asymmetry is, of course, also reflected in the structures of the radial velocity. By comparing the left and right panels in figure 7a, it can be seen that the increase in polymer stretch taking place in the lower half of the arrows is associated with shear layers that form in the boundaries between inflows and outflows. These shear layers are readily identified in the figure as regions where the contours of radial velocity are closely spaced, thereby indicating strong velocity gradients.

The AArrowRW is stable in a narrow range of  $Wi$  numbers,  $17.3 \lesssim Wi \lesssim 18.4$  for  $Re = 100$  (see blue diamonds in figure 4b). Within this range, the symmetrically related state, AArrowRW\* =  $K_z$ AArrowRW, has also been found (not shown). It has the same characteristics as the AArrowRW state, but shear layers and higher polymer stretch are in this case observed in the upper half of the arrow-shaped structures. It should also be noted that, unlike the ArrowRW state, the kinetic energy of the AArrowRW decreases monotonically as  $Wi$  increases. Following the solution beyond  $Wi \gtrsim 18.4$ , the flow becomes chaotic and the kinetic energy decreases markedly (see states denoted by (orange) cross marks in figure 4b). Irregular arrow-shaped structures are transiently observed in the polymer stretch field, coexisting with strips of highly stretched polymers that extend over the entire azimuthal length (see figure 7b). Unlike the flow states described above, arrow-shaped structures appear at random  $\theta$  and  $z$  locations and their azimuthal extent is highly variable. Due to this randomness, the property that the structures are shifted by half a wavelength every half a rotation period is evidently absent. This chaotic flow is consistent with a state of DO, which is the term used in viscoelastic TCF to denote chaotic flow patterns characterized by large-scale irregular flow structures [15,21–28]. This is, however, the first time that a DO state with arrow-shaped structures is reported.

Another flow state where arrow-shaped structures also appear is found at low  $Re$  values, near the saddle-node bifurcation point of the ArrowRW (see (red) squares in 4a). Such a state, which is presented in figure 7c for  $Re = 30$  and  $Wi = 15$ , exhibits axially symmetric arrow-shaped structures of polymer stretch which are similar in length and magnitude to those of the ArrowRW. However, they appear only in one half of the system, i.e. over half a rotation period. We have dubbed this flow state as localized arrow-shaped rotating wave (LArrowRW). We would like to note that localization of structures in TCF usually happens in the axial direction or in both axial and azimuthal directions, resulting in patches. The azimuthal localization observed in this viscoelastic flow state is thus quite unusual and the mechanism behind it is still not understood. The parameter range in which the LArrowRW state exists is smaller than that for the ArrowRW state, for both  $Re$  and  $Wi$  numbers (see (red) squares in figure 4). When  $Wi = 15$ , the minimum  $Re$  value up to which the LArrowRW can be followed is  $Re \approx 16.5$ , where the flow recovers its laminarity, whereas the highest  $Re$  value at which this state exists is  $Re \approx 45$ . Beyond this value, this solution branch becomes unstable and the simulations converge to the ArrowRW state. When the flow pattern is continued in  $Wi$ , while keeping  $Re = 30$ , the flow laminarizes below  $Wi \approx 11.5$ . The kinetic energy of the LArrowRW increases monotonically with increasing  $Wi$  (states with nearly constant energy have not been found for this solution) until at  $Wi \approx 23$ , this solution loses stability to the ArrowRW.

Flow structures which do not exhibit arrow-shaped structures have also been found at low  $Wi$  numbers. These are well-known structures of TCF, the so-called SP and RB states [2,5]. SP are found to exist when  $0.5 \lesssim Wi \lesssim 6.5$ , whereas RB exist in a narrower region,  $1.5 \lesssim Wi \lesssim 3.5$  (see figure 4b). These flow patterns have been widely analysed in the literature and will not be further discussed here.

## 6. Conclusion

Using direct numerical simulations of the governing equations, we have demonstrated the existence of axially localized, arrow-shaped structures of polymer stretch in the TCF of a dilute

polymer solution. These structures have been identified in both rotating waves and in disordered flow patterns. An analysis of the integral energy balance has revealed that stable arrow-shaped rotating waves occur when the energy input associated with elastic mechanisms is the leading order term. In contrast, when the elastic and inertial contributions are comparable, these solutions become unstable.

Recently, arrow-shaped regions of highly stretched polymers have also been identified in viscoelastic channel flow at elasticity levels similar to those investigated here. Despite these structures being qualitatively distinct from those we report, it is interesting to note that in both cases they are aligned with the mean flow direction (the azimuthal direction in TCF and the axial direction in channels). This observation appears to support the hypothesis in [37] that arrow-shaped structures are caused by an increase in the elongational viscosity of the flow due to polymer stretching in the primary flow direction, and it suggests that they could exist in any viscoelastic fluid flow where there is a dominant velocity component.

Among the rotating waves found in the study, the LArrowRW state, where the arrow-shaped structures are only found in half of the system, is particularly interesting. Further research is needed to understand the mechanism behind this surprising feature. It also remains to see if these rotating waves persist in a real TCF system, where the assumption of axial periodicity adopted in our study is not fulfilled. Simulations with axial boundary conditions mimicking the experimental end-plates and/or laboratory experiments will be needed to answer this question. It should be noted that although the polymer stretch field cannot be easily measured in experiments, we have shown that another distinctive feature of these rotating waves is that the radial velocity structures are also arrow headed and point in the flow direction. Since the temporal evolution of the rotating wave pattern is equivalent to its azimuthal dependence, a space–time plot of the radial velocity obtained at the mid-gap and at constant  $\theta$ , over a rotation period, would be identical to the cylindrical sections presented in this paper. This characteristic could hence be used to detect these structures in experiments.

Despite its age and extensive research, the classical TCF setup (inner cylinder rotating and outer cylinder at rest) offers a great opportunity to detect previously unknown states. This is especially true when non-Newtonian fluids, such as viscoelastic fluids, are used as working fluids, further expanding the problem's already large parameter space.

**Data accessibility.** The datasets supporting this article are available as part of the electronic supplementary material [48]. The data that support the findings of this study are available from the authors upon reasonable request.

**Authors' contributions.** J.M.L.: conceptualization, data curation, formal analysis, funding acquisition, investigation, methodology, software, validation, visualization, writing—original draft, writing—review and editing; S.A.A.: conceptualization, data curation, formal analysis, funding acquisition, investigation, methodology, validation, visualization, writing—original draft, writing—review and editing.

All authors gave final approval for publication and agreed to be held accountable for the work performed therein.

**Conflict of interest declaration.** We declare we have no competing interests.

**Funding.** This work was supported by the two Spanish Ministerio de Ciencia e Innovación grants PID2019-105162RB-I00 and PID2020-114043GB-100.

**Acknowledgements.** The authors thankfully acknowledge the computer resources at Pirineus and the technical support provided by the Consorci de Serveis Universitari de Catalunya (RES-IM-2022-1-0005).

## References

1. Taylor GI. 1923 Stability of a viscous liquid contained between two rotating cylinders. *Phil. Trans. R. Soc. Lond. A* **223**, 289–343. ([doi:10.1098/rsta.1923.0008](https://doi.org/10.1098/rsta.1923.0008))
2. Chossat P, Iooss G. 1994 *The Couette-Taylor problem*. Berlin: Springer.
3. Tagg R. 1994 The Couette-Taylor problem. *Nonlinear Sci. Today* **4**, 1.
4. Langford WF, Tagg R, Kostelich EJ, Swinney HL, Golubitsky M. 1988 Primary instabilities and bicriticality in flow between counter rotating cylinders. *Phys. Fluids* **31**, 776–785. ([doi:10.1063/1.866813](https://doi.org/10.1063/1.866813))

5. Andereck CD, Liu SS, Swinney HL. 1986 Flow regimes in a circular Couette system with independently rotating cylinders. *J. Fluid Mech.* **164**, 155–183. ([doi:10.1017/S0022112086002513](https://doi.org/10.1017/S0022112086002513))
6. Jones CA. 1981 Nonlinear Taylor vortices and their stability. *J. Fluid Mech.* **102**, 249–261. ([doi:10.1017/S0022112081002620](https://doi.org/10.1017/S0022112081002620))
7. Jones CA. 1985 The transition to wavy Taylor vortices. *J. Fluid Mech.* **157**, 135–162. ([doi:10.1017/S0022112085002336](https://doi.org/10.1017/S0022112085002336))
8. King GP, Lee YL, Marcus PS. 1984 Wave speeds in wavy Taylor-vortex flow. *J. Fluid Mech.* **141**, 365–390. ([doi:10.1017/S0022112084000896](https://doi.org/10.1017/S0022112084000896))
9. Wereley ST, Lueptow RM. 1998 Spatio-temporal character of non-wavy and wavy Taylor-Couette flow. *J. Fluid Mech.* **364**, 59–80. ([doi:10.1017/S0022112098008969](https://doi.org/10.1017/S0022112098008969))
10. Martinand D, Serre E, Lueptow RM. 2014 Mechanisms for the transition to waviness for Taylor vortices. *Phys. Fluids* **26**, 094102. ([doi:10.1063/1.4895400](https://doi.org/10.1063/1.4895400))
11. Dessup T, Tuckerman LS, Wesfreid JE, Barkley D, Willis AP. 2018 Self-sustaining process in Taylor-Couette flow. *Phys. Rev. Fluids* **3**, 123902. ([doi:10.1103/PhysRevFluids.3.123902](https://doi.org/10.1103/PhysRevFluids.3.123902))
12. Muller SJ, Larson RG, Shaqfeh ES. 1989 A purely elastic transition in Taylor-Couette flow. *Rheol. Acta* **28**, 499–503. ([doi:10.1007/BF01332920](https://doi.org/10.1007/BF01332920))
13. Larson RG, Shaqfeh ESG, Muller SJ. 1990 A purely elastic instability in Taylor-Couette flow. *J. Fluid Mech.* **218**, 573–600. ([doi:10.1017/S0022112090001124](https://doi.org/10.1017/S0022112090001124))
14. Shaqfeh ESG. 1996 Purely elastic instabilities in viscometric flows. *Annu. Rev. Fluid Mech.* **28**, 129–185. ([doi:10.1146/annurev.fl.28.010196.001021](https://doi.org/10.1146/annurev.fl.28.010196.001021))
15. Groisman A, Steinberg V. 1996 Couette-Taylor flow in a dilute polymer solution. *Phys. Rev. Lett.* **77**, 1480–1483. ([doi:10.1103/PhysRevLett.77.1480](https://doi.org/10.1103/PhysRevLett.77.1480))
16. Crumeyrolle O, Mutabazi I, Grisel M. 2002 Experimental study of inertioelastic Couette-Taylor instability modes in dilute and semidilute polymer solutions. *Phys. Fluids* **14**, 1681–1688. ([doi:10.1063/1.1466837](https://doi.org/10.1063/1.1466837))
17. Groisman A, Steinberg V. 1997 Solitary vortex pairs in viscoelastic Couette flow. *Phys. Rev. Lett.* **78**, 1460–1463. ([doi:10.1103/PhysRevLett.78.1460](https://doi.org/10.1103/PhysRevLett.78.1460))
18. Baumert BM, Muller SJ. 1997 Flow regimes in model viscoelastic fluids in a circular Couette system with independently rotating cylinders. *Phys. Fluids* **9**, 566–586. ([doi:10.1063/1.869209](https://doi.org/10.1063/1.869209))
19. Baumert BM, Muller SJ. 1999 Axisymmetric and non-axisymmetric elastic and inertio-elastic instabilities in Taylor-Couette flow. *J. Nonnewton. Fluid Mech.* **83**, 33–69. ([doi:10.1016/S0377-0257\(98\)00132-3](https://doi.org/10.1016/S0377-0257(98)00132-3))
20. Latrache N, Mutabazi I. 2021 Transition to turbulence via flame patterns in viscoelastic Taylor-Couette flow. *Eur. Phys. J. E* **44**, 63. ([doi:10.1140/epje/s10189-021-00067-0](https://doi.org/10.1140/epje/s10189-021-00067-0))
21. Latrache N, Abcha N, Crumeyrolle O, Mutabazi I. 2016 Defect-mediated turbulence in ribbons of viscoelastic Taylor-Couette flow. *Phys. Rev. E* **93**, 043126. ([doi:10.1103/PhysRevE.93.043126](https://doi.org/10.1103/PhysRevE.93.043126))
22. Samanta D, Dubief Y, Holzner M, Schäfer C, Morozov AN, Wagner C, Hof B. 2013 Elasto-inertial turbulence. *Proc. Natl Acad. Sci. USA* **110**, 10557–10562. ([doi:10.1073/pnas.1219666110](https://doi.org/10.1073/pnas.1219666110))
23. Dubief YT. 2013 On the mechanism of elasto-inertial turbulence. *Phys. Fluids* **25**, 110817. ([doi:10.1063/1.4820142](https://doi.org/10.1063/1.4820142))
24. Sid S, Terrapon VE, Dubief Y. 2018 Two-dimensional dynamics of elasto-inertial turbulence and its role in polymer drag reduction. *Phys. Rev. Fluids* **3**, 011301. ([doi:10.1103/PhysRevFluids.3.011301](https://doi.org/10.1103/PhysRevFluids.3.011301))
25. Shekar A, McMullen RM, Wang SN, McKeon BJ, Graham MD. 2019 Critical-layer structures and mechanisms in elastoinertial turbulence. *Phys. Rev. Lett.* **122**, 124503. ([doi:10.1103/PhysRevLett.122.124503](https://doi.org/10.1103/PhysRevLett.122.124503))
26. Thomas DG, Khomami B, Sureshkumar R. 2009 Nonlinear dynamics of viscoelastic Taylor-Couette flow: effect of elasticity on pattern selection, molecular conformation and drag. *J. Fluid Mech.* **620**, 353–382. ([doi:10.1017/S0022112008004710](https://doi.org/10.1017/S0022112008004710))
27. Thomas DG, Sureshkumar R, Khomami B. 2006 Pattern formation in Taylor-Couette flow of dilute polymer solutions: dynamical simulations and mechanism. *Phys. Rev. Lett.* **97**, 054501. ([doi:10.1103/PhysRevLett.97.054501](https://doi.org/10.1103/PhysRevLett.97.054501))
28. Liu N, Khomami B. 2013 Elastically induced turbulence in Taylor-Couette flow: direct numerical simulation and mechanistic insight. *J. Fluid Mech.* **737**, R4. ([doi:10.1017/jfm.2013.544](https://doi.org/10.1017/jfm.2013.544))

29. Song J, Lin F, Liu N, Lu X-Y, Khomami B. 2021 Direct numerical simulation of inertio-elastic turbulent Taylor–Couette flow. *J. Fluid Mech.* **926**, A37. ([doi:10.1017/jfm.2021.757](https://doi.org/10.1017/jfm.2021.757))
30. Song J, Teng H, Liu N, Ding H, Lu X-Y, Khomami B. 2019 The correspondence between drag enhancement and vortical structures in turbulent Taylor–Couette flows with polymer additives: a study of curvature dependence. *J. Fluid Mech.* **881**, 602–616. ([doi:10.1017/jfm.2019.760](https://doi.org/10.1017/jfm.2019.760))
31. Lacassagne T, Cagney N, Balabani S. 2021 Shear-thinning mediation of elasto-inertial Taylor–Couette flow. *J. Fluid Mech.* **915**, A91. ([doi:10.1017/jfm.2021.104](https://doi.org/10.1017/jfm.2021.104))
32. Lacassagne T, Cagney N, Gillissen JJJ, Balabani S. 2020 Vortex merging and splitting: a route to elastoinertial turbulence in Taylor–Couette flow. *Phys. Rev. Fluids* **5**, 113303. ([doi:10.1103/PhysRevFluids.5.113303](https://doi.org/10.1103/PhysRevFluids.5.113303))
33. Cagney N, Lacassagne T, Balabani S. 2020 Taylor–Couette flow of polymer solutions with shear-thinning and viscoelastic rheology. *J. Fluid Mech.* **905**, A28. ([doi:10.1017/jfm.2020.701](https://doi.org/10.1017/jfm.2020.701))
34. Lopez Jose M. 2022 Vortex merging and splitting events in viscoelastic Taylor–Couette flow. *J. Fluid Mech.* **946**, A27.
35. Song J, Wan Z-H, Liu N, Lu X-Y, Khomami B. 2021 A reverse transition route from inertial to elasticity-dominated turbulence in viscoelastic Taylor–Couette flow. *J. Fluid Mech.* **927**, A10. ([doi:10.1017/jfm.2021.728](https://doi.org/10.1017/jfm.2021.728))
36. Page J, Dubief Y, Kerswell RR. 2020 Exact traveling wave solutions in viscoelastic channel flow. *Phys. Rev. Lett.* **125**, 154501. ([doi:10.1103/PhysRevLett.125.154501](https://doi.org/10.1103/PhysRevLett.125.154501))
37. Dubief Y, Page J, Kerswell RR, Terrapon VE, Steinberg V. 2022 First coherent structure in elasto-inertial turbulence. *Phys. Rev. Fluids* **7**, 073301. ([doi:10.1103/PhysRevFluids.7.073301](https://doi.org/10.1103/PhysRevFluids.7.073301))
38. Bird R, Dotson P, Johnson N. 1980 Polymer solution rheology based on a finitely extensible bead-spring chain model. *J. Nonnewton. Fluid Mech.* **7**, 213–235. ([doi:10.1016/0377-0257\(80\)85007-5](https://doi.org/10.1016/0377-0257(80)85007-5))
39. Song J, Teng H, Liu N, Ding H, Lu X-Y, Khomami B. 2019 The correspondence between drag enhancement and vortical structures in turbulent Taylor–Couette flows with polymer additives: a study of curvature dependence. *J. Fluid Mech.* **881**, 602–616. ([doi:10.1017/jfm.2019.760](https://doi.org/10.1017/jfm.2019.760))
40. Lopez JM, Feldmann D, Rampp M, Vela-Martin A, Shi L, Avila M. 2020 nsCouette—a high-performance code for direct numerical simulations of turbulent Taylor–Couette flow. *SoftwareX* **11**, 100395.
41. Lopez JM, Choueiri GH, Hof B. 2019 Dynamics of viscoelastic pipe flow at low Reynolds numbers in the maximum drag reduction limit. *J. Fluid Mech.* **874**, 699–719. ([doi:10.1017/jfm.2019.486](https://doi.org/10.1017/jfm.2019.486))
42. Willis AP. 2017 The openpipeflow Navier–Stokes solver. *SoftwareX* **6**, 124–127. ([doi:10.1016/j.softx.2017.05.003](https://doi.org/10.1016/j.softx.2017.05.003))
43. Buza G, Page J, Kerswell R. 2022 Weakly nonlinear analysis of the viscoelastic instability in channel flow for finite and vanishing Reynolds numbers. *J. Fluid Mech.* **940**, A11. ([doi:10.1017/jfm.2022.222](https://doi.org/10.1017/jfm.2022.222))
44. Choueiri GH, Lopez JM, Varshney A, Sankar S, Hof B. 2021 Experimental observation of the origin and structure of elastoinertial turbulence. *Proc. Natl Acad. Sci. USA* **118**, e2102350118. ([doi:10.1073/pnas.2102350118](https://doi.org/10.1073/pnas.2102350118))
45. Groisman A, Steinberg V. 1998 Mechanism of elastic instability in Couette flow of polymer solutions: experiment. *Phys. Fluids* **10**, 2451–2463. ([doi:10.1063/1.869764](https://doi.org/10.1063/1.869764))
46. Itano T, Toh S. 2001 The dynamics of bursting process in wall turbulence. *J. Phys. Soc. Jpn* **70**, 703–716. ([doi:10.1143/JPSJ.70.703](https://doi.org/10.1143/JPSJ.70.703))
47. Dallas V, Vassilicos JC, Hewitt GF. 2010 Strong polymer-turbulence interactions in viscoelastic turbulent channel flow. *Phys. Rev. E* **82**, 066303. ([doi:10.1103/PhysRevE.82.066303](https://doi.org/10.1103/PhysRevE.82.066303))
48. Lopez JM, Altmeyer SA. 2023 Arrow-shaped elasto-inertial rotating waves. Figshare. ([doi:10.6084/m9.figshare.c.6412326](https://doi.org/10.6084/m9.figshare.c.6412326))